

# Enhancing the Interfacial Stability of High-Energy Si/Graphite || LiNi<sub>0.88</sub>Co<sub>0.09</sub>Mn<sub>0.03</sub>O<sub>2</sub> Batteries Employing a Dual-Anion Ionic Liquid-based Electrolyte

Shan Fang,<sup>[a, b, c]</sup> Fanglin Wu,<sup>[b, c]</sup> Maider Zarabeitia,<sup>[b, c]</sup> Matthias Kuenzel,<sup>[b, c]</sup> Daniel Roscher,<sup>[b, c]</sup> Xinpei Gao,<sup>[b, c]</sup> Jae-Kwang Kim,<sup>[d]</sup> Guk-Tae Kim,<sup>\*[b, c]</sup> and Stefano Passerini<sup>\*[b, c]</sup>

The poorly flammable room-temperature ionic liquid-based electrolyte composed of lithium bis(trifluoromethanesulfonyl)imide (LiTFSI) and N-butyl-N-methylpyrrolidinium bis(fluorosulfonyl)imide (Pyr<sub>14</sub>FSI) with fluoroethylene carbonate (FEC) as an additive is investigated towards its compatibility with the LiNi<sub>0.88</sub>Co<sub>0.09</sub>Mn<sub>0.03</sub>O<sub>2</sub> (NCM88) cathode and a high-capacity Si/graphite (SiG) anode, revealing a remarkably stable performance in lithium-ion cells. Interestingly, this dual-anion electrolyte with FEC additive forms a stable electrode-electrolyte interphase on both sides, which sup-

presses the morphological degradation of the electrode materials and continuous electrolyte decomposition. Consequently, lithium-ion cells using such dual-anion ionic liquid-based electrolyte display significantly improved cycling stability compared to conventional carbonate ester-based electrolyte, achieving a high specific energy of 385 Wh kg<sup>-1</sup> (based on both cathode and anode active materials weight) with a capacity retention of 74% after 200 cycles at 0.2 C, demonstrating the possibility to realize safe and high energy density LIBs.

## Introduction

High energy density lithium-ion batteries (LIBs) are required to increase the driving range of electric vehicles. Thus, selecting advanced electrode materials with high specific (theoretical) capacity is the simplest approach to improve the energy density of LIBs.<sup>[1,2]</sup> At the negative electrode, to avoid the safety risks posed by using metallic lithium,<sup>[3]</sup> silicon is considered the best candidate to replace graphite. Silicon has an almost ten times higher specific capacity than graphite (3579 mAh g<sup>-1</sup>), is less expensive and far more abundant in the Earth's crust. In

addition, the average lithiation potential of Si is lower than 0.4 V vs. Li<sup>+</sup>/Li, which is slightly higher than graphite (0.1 V vs. Li<sup>+</sup>/Li), thus reducing the risk of lithium plating and dendrite formation during cycling especially at high charge rates and at a relatively low energy penalty.<sup>[4–6]</sup> However, the main challenge of Si anodes is their large volume expansion during lithiation, resulting in unstable and excessive solid electrolyte interphase (SEI) formation and particle pulverisation. This leads to a rapid capacity fading of pure Si anodes and hinders their practical implementation.<sup>[6,7]</sup> The main strategies to counter this are the modification of Si by designing nanostructures,<sup>[8]</sup> coating the material with carbon,<sup>[9,10]</sup> or using functional binders with high modulus to buffer the volume changes.<sup>[11,12]</sup> However, from a practical perspective, the incorporation of only small amounts (3–5 wt.-%<sup>[13]</sup>) of Si in composites with graphite has been considered the most efficient to increase the capacity and energy density, as well as retaining the high stability of graphite electrodes; this has been introduced for commercial LIBs.<sup>[14]</sup>

For the positive electrode, Ni-rich layered oxide materials (LiNi<sub>x</sub>Mn<sub>y</sub>Co<sub>z</sub>O<sub>2</sub>,  $x \geq 0.6$ ,  $x+y+z=1$ , NCM) are currently the preferred choice for high-energy LIBs, following the trend towards increasingly high Ni contents to reduce the amount of critical and toxic cobalt and increase the specific capacity ( $\geq 170$  mAh g<sup>-1</sup>).<sup>[15,16]</sup> Nevertheless, very high nickel contents ( $x \geq 0.8$ ) also introduce safety concerns and reduce the cycle life of the cells, because of severe parasitic side reactions with the electrolyte as well as structural and morphological degradation of the cathode material at high state of charge.<sup>[17,18]</sup> The oxidative decomposition of the electrolyte in combination with the highly reactive Ni<sup>4+</sup> present in the charged state lowers the

[a] Dr. S. Fang  
School of Physics and Materials  
Nanchang University  
Nanchang, Jiangxi, 330031, China

[b] Dr. S. Fang, Dr. F. Wu, Dr. M. Zarabeitia, Dr. M. Kuenzel, D. Roscher, Dr. X. Gao, Dr. G.-T. Kim, Prof. Dr. S. Passerini  
Helmholtz Institute Ulm (HIU)  
Helmholtzstrasse 11, Ulm 89081, Germany  
E-mail: guk-tae.kim@kit.edu  
stefano.passerini@kit.edu

[c] Dr. S. Fang, Dr. F. Wu, Dr. M. Zarabeitia, Dr. M. Kuenzel, D. Roscher, Dr. X. Gao, Dr. G.-T. Kim, Prof. Dr. S. Passerini  
Karlsruhe Institute of Technology (KIT)  
P.O. Box 3640, Karlsruhe 76021, Germany

[d] Prof. J.-K. Kim  
Department of Energy Convergence Engineering  
Cheongju University  
Cheongju, Chungbuk, 28503, Republic of Korea

 Supporting information for this article is available on the WWW under  
<https://doi.org/10.1002/batt.202200286>

 © 2022 The Authors. *Batteries & Supercaps* published by Wiley-VCH GmbH. This is an open access article under the terms of the Creative Commons Attribution License, which permits use, distribution and reproduction in any medium, provided the original work is properly cited.

thermal stability of the material. In addition, the similar ionic radius of  $\text{Li}^+$  (0.076 nm) and  $\text{Ni}^{2+}$  (0.069 nm) results in an intermixing of Ni and Li ions in the structure, promoting the phase transition from the layered to the electrochemically inactive rock-salt structure.<sup>[19,20]</sup> Additionally, the large variation of unit cell volume generates mechanical stress on the secondary particles. During repeated cycling, cracks are formed rapidly causing the penetration of electrolyte into the secondary particles, where the detrimental side-reactions are triggered, accelerating the structure deterioration and voltage decay.<sup>[21,22]</sup> Thus, the application of these materials in lithium-ion cells remains challenging, especially because of the formation of unstable cathode electrolyte interphases (CEI) and thermal instability.

Recently, a safety improvement was achieved using room temperature, non-volatile and poorly flammable ionic liquid electrolytes (ILEs) specifically with respect to Ni-rich cathodes, achieving excellent long-term cycling stability.<sup>[23,24]</sup> Heist et al.<sup>[23]</sup> employed a bis(fluorosulfonyl) imide (FSI)-based ILE for Ni-rich cathodes ( $\text{LiNi}_{0.8}\text{Mn}_{0.1}\text{Co}_{0.1}\text{O}_2$ ) for the first time and obtained satisfactory electrochemical performance. In our previous work, a dual-anion ILE consisting of bis(fluorosulfonyl) imide (FSI) and bis(trifluoromethanesulfonyl)imide (TFSI) was successfully applied to enhance the stability of highly Ni-rich layered oxide cathodes ( $\text{LiNi}_{0.88}\text{Co}_{0.09}\text{Mn}_{0.03}\text{O}_2$ , NCM88), achieving an outstanding capacity retention of 88% over 1,000 cycles in lithium-metal batteries (LMBs).<sup>[24]</sup> Although these ILEs reportedly inhibit surface degradation of Ni-rich NCM layered cathodes, they are mostly used in lithium-metal cells due to the frequently observed incompatibility of ILEs with graphite.<sup>[25]</sup> Using ILEs with Si/graphite (SiG) negative electrodes is similarly challenging because the organic cations may insert into graphite, partially leading to its decomposition due to exfoliation resulting in decreased battery performance and the formation of unstable SEI.<sup>[26,27]</sup> Herein, for the first time, we successfully

realized the combination of SiG composite negative and Ni-rich NCM88 positive electrodes in lithium-ion cells employing a safe poorly-flammable dual-anion ionic liquid-based electrolyte. The comparative study of the two slightly different ILEs based on the  $\text{Pyr}_{14}^+$  cation and the  $\text{FSI}^-$  anion as solvents, investigates LiTFSI and LiFSI as Li salt, with fluoroethylene carbonate (FEC) as additives to achieve stable cycling of  $\text{SiG} \parallel \text{NCM88}$  lithium-ion cells. Remarkably, choosing the right ILE, highly stable electrode-electrolyte interphases are formed on both electrodes (SEI and CEI) and the  $\text{SiG} \parallel \text{NCM88}$  lithium-ion cell shows a high specific energy of  $385 \text{ Wh kg}^{-1}$  (based on both cathode and anode active materials weights) with a capacity retention of 74% after 200 cycles.

## Results and Discussion

The morphology of the SiG (Figure S1) and the NCM88 (Figure S2) active materials was characterised by scanning electron microscopy (SEM). Most of the 5–10  $\mu\text{m}$  sized Si particles are evenly distributed among the graphite, with only a few particles of significantly smaller size ( $< 1 \mu\text{m}$ ) visible. The NCM88 is mostly composed of secondary particles of a spherical morphology with the particle size in the range of 2 to 15  $\mu\text{m}$ . Higher magnification SEM image indicates that the primary particles have an irregular rod-like shape and are tightly packed together (see Figure S2b). Prior to lithium-ion cell assembly, the electrochemical performance of SiG negative electrodes and NCM88 positive electrodes has been evaluated in half-cells using a conventional organic carbonate ester-based electrolyte (1 M  $\text{LiPF}_6$  in EC/DEC + 10 wt.% FEC + 1 wt.% VC, labelled as OR) as shown in Figure 1. The first dis-/charge capacity of SiG is  $501.0/625.6 \text{ mAh g}^{-1}$  at 0.1 C (1 C =  $600 \text{ mA g}^{-1}$ ), corresponding to an initial Coulombic efficiency (ICE) of 80%. The relatively low ICE (compared to pure graphite)

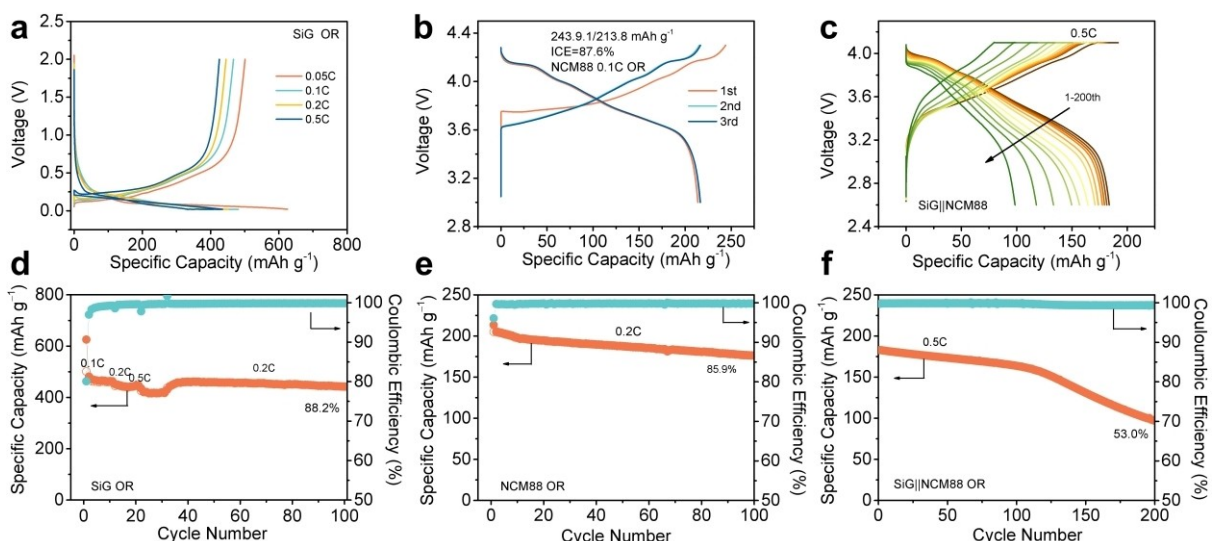


**Figure 1.** a–c) Selected voltage profiles and d–f) galvanostatic cycling of a, d) SiG and b, e) NCM88 in half-cells configuration as well as c, f)  $\text{SiG} \parallel \text{NCM88}$  lithium-ion cells in organic carbonate ester-based electrolyte (1 M  $\text{LiPF}_6$  in EC/DEC + 10 wt.% FEC + 1 wt.% VC, labelled as OR). The specific capacity values refer to the weight of the electrode material under investigation in half-cells (SiG or NCM88), but to the weight of NCM88 only for the full-cell tests.

is due to the irreversibility of Li alloying with Si and the electrolyte decomposition forming the SEI.<sup>[28]</sup> Figure 1d shows the rate capability and cycling performance of SiG in half-cells at initially 10 cycles each at 0.1 C, 0.2 C, and 0.5 C, before continuous cycling at 0.2 C. The capacity retention is 88.2% after 100 cycles with an average Coulombic efficiency (CE) of 99.6% (not considering the ICE). The electrochemical performance of NCM88 in half-cells is shown in Figure 1(b and e). The first dis-/charge capacity is 213.8/243.9 mAh g<sup>-1</sup> at 0.1 C (1 C = 200 mA g<sup>-1</sup>) in a voltage range of 3.0–4.3 V vs. Li<sup>+</sup>/Li. After three formation cycles at 0.1 C, the NCM88 half-cell is continuously cycled at 0.2 C for 100 cycles, showing a capacity retention of 85.9% and an average CE of 99.7%. To achieve stable and high energy SiG || NCM88 lithium-ion cells, the voltage window was set to 2.6–4.1 V. Considering the formation of SEI and CEI on the electrodes during the first cycle and the excess consumption of Li ions from electrolyte and cathode, the SiG anode was pre-lithiated to 0.25 V (~60 mAh g<sup>-1</sup>), and then assembled against the NCM88 positive electrode.<sup>[27]</sup> Figure S3 presents typical voltage profiles of the lithium-ion cell during initial cycles. The specific dis-/charge capacity of the first cycle is 195.2/220.6 mAh g<sup>-1</sup>, corresponding to an ICE of 88.5%. The irreversible capacity loss may still be due to electrolyte decomposition and SEI/CEI formation on both electrodes. The specific energy of such cells tested in OR electrolyte is 458 Wh kg<sup>-1</sup>, based on the cathode and anode active material weights. Figure 1(c and f) shows the evolution of voltage profiles and cycling performance of the SiG || NCM88 cell cycled at 0.5 C in the voltage range of 2.6–4.1 V. The SiG || NCM88 cell delivers 86% of the initial capacity after 100 cycles with an average CE of 99.9%. However, the capacity fades rapidly during the following cycles indicating the Li-reservoir from pre-

lithiation of the anode has been consumed in the early stages of cycling. After 200 cycles, the capacity retention is only 53% and the average CE decreased to 99.7%. In addition, the voltage profiles show increasingly high polarisation. The severe capacity fading during long-term cycling is mainly caused by the large volume expansion and particle pulverisation of Si during repeated lithiation, causing the continuous reaction with electrolyte and resulting in a thick SEI that increases cell resistance.<sup>[6,7]</sup> This is additionally amplified by the instability of the NCM88 CEI in organic carbonate ester-based electrolytes, and cathode material degradation at high state of charge.<sup>[24,29,30]</sup>

To fully exploit the great potential of the individual electrode materials, and at the same time improve the safety and electrochemical performance of SiG || NCM88 lithium-ion cells, we aimed to replace the OR electrolyte by poorly flammable ILEs [0.8 mol Pyr<sub>14</sub>FSI-0.2 mol LiFSI + 10 wt.% FEC (ILE1) and 0.8 mol Pyr<sub>14</sub>FSI-0.2 mol LiTFSI + 10 wt.% FEC (ILE2)], with FEC as an SEI stabilising additive for the SiG negative electrode.<sup>[31,32]</sup> The electrochemical stability window of the ILEs was determined by linear sweep voltammetry (LSV) shown in Figure 2(a). The ILE with exclusively FSI<sup>-</sup> anions (ILE1) displays a steeper rise of the anodic current than the dual-anion electrolyte (ILE2) with additional TFSI<sup>-</sup> anions, with a slightly higher anodic stability. The ionic conductivity of the two ILEs is displayed in Figure 2(b). ILE1 exhibits slightly higher ionic conductivity, from 18 mS cm<sup>-1</sup> at 80 °C to 0.5 mS cm<sup>-1</sup> at -20 °C. Meanwhile the ionic conductivity values of ILE2 range from 15 mS cm<sup>-1</sup> at 80 °C to 0.3 mS cm<sup>-1</sup> at -20 °C. The lower ionic conductivity of ILE2 is due to the large molecular size of TFSI<sup>-</sup> compared to FSI<sup>-</sup>, which increases the viscosity and glass transition, and thus decreases the conductivity of the electrolyte.<sup>[33]</sup> Nevertheless, the room temperature ionic con-

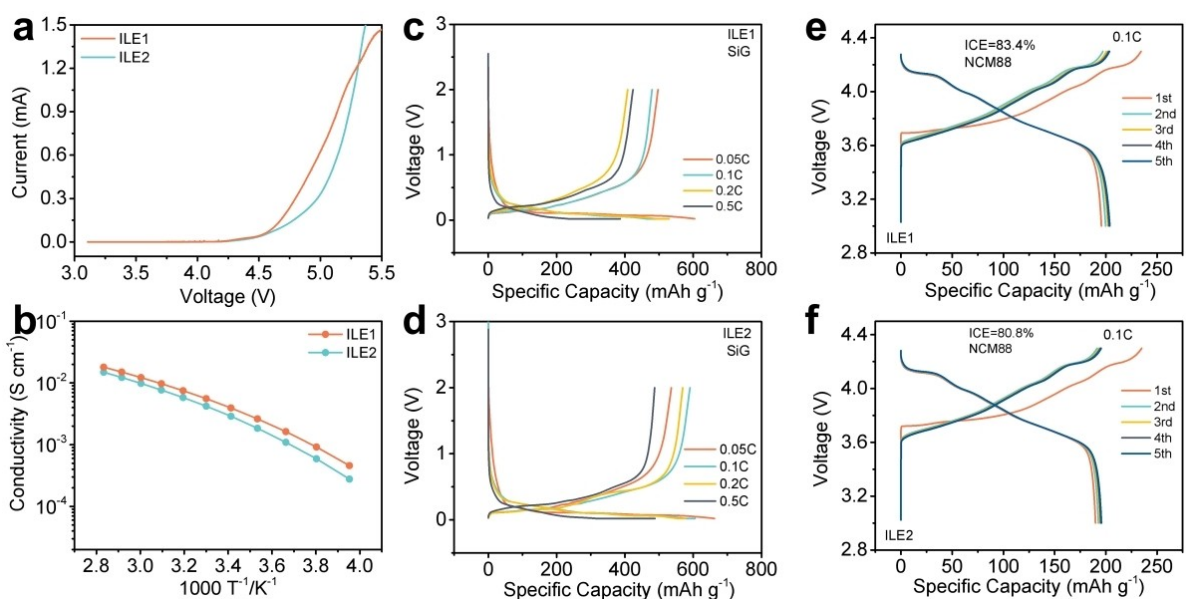


**Figure 2.** a) Linear sweep voltammetry to probe the electrochemical stability window of ILE1 and ILE2 recorded at a scan rate of 0.1 mV s<sup>-1</sup> using a Ni foil as working electrode. b) Ionic conductivity of both ILEs. c, d) Selected voltage profiles of SiG half-cells in ILE1 and ILE2, respectively. Voltage profiles during the first five cycles of NCM88 half-cells at 0.1 C in e) ILE1 and f) ILE2. The specific capacity values refer to the weight of the electrode material under investigation in half-cells (SiG or NCM88).

ductivity of ILE1 and ILE2 is in the same order of magnitude as the organic electrolyte ( $7 \times 10^{-3}$ – $8 \times 10^{-3} \text{ S cm}^{-1}$ <sup>[34]</sup>), i.e., suitable for application. To provide further insight regarding the compatibility of the ILEs towards the anode and its SEI forming capability, cyclic voltammograms (CVs) were recorded for SiG electrodes in both ILEs as shown in Figure S4. The CV curves show the typical features related to alloying and de-alloying of Li with Si. The corresponding cathodic peak is observed at 0.2 V and the anodic peaks appear at 0.31 and 0.5 V.<sup>[35]</sup> Moreover, the pronounced anodic feature located at 0.2 V represents the Li extraction from graphite.<sup>[29]</sup> The CV results indicate that the ILEs and graphite have good compatibility, and no other cathodic features which would indicate  $\text{Pyr}_{14}^{+}$  cation intercalation into graphite are observed. Figure 2(c and d) shows the charge/discharge curves of SiG half-cells in these two electrolytes, with very similar electrochemical performance as in OR electrolyte (Figure 1). The first specific dis-/charge (delithiation/lithiation) capacity in ILE1 is  $496.8/604.3 \text{ mAh g}^{-1}$ , which is slightly lower than that observed in ILE2 ( $535.9/662.7 \text{ mAh g}^{-1}$ ). The cycling stability of the SiG electrode has been assessed using the same procedure as in OR electrolyte. The results further confirm the good compatibility of both ILEs with graphite. After 100 cycles at 0.2 C, the capacity retention is 76% in ILE1 and 82% in ILE2, respectively (based on the first cycle reversible capacity at 0.05 C; Figure S5). The higher specific capacity and more stable cycling performance was obtained for the dual-anion electrolyte containing  $\text{FSI}^-$  and  $\text{TFSI}^-$  anions (ILE2). This might be ascribed to the well-maintained integrity of SiG particles cycled in ILE2 electrolyte, facilitated through a protective and stable SEI on the surface of Si and graphite. The decomposition mechanisms of  $\text{FSI}^-$  and  $\text{TFSI}^-$  upon electrochemical reduction differ,<sup>[33,36,37]</sup> resulting in different chemical composition and morphology of the IL-derived SEI. In relation to the interaction

of ILEs with the positive electrode, Figure 2(e and f) compares the electrochemical performance of NCM88 half-cells in the different ILEs. In both cases, NCM88 has its typical discharge/charge profile and similar specific capacity. Considering our previous work, this is not surprising as excellent long-term cycling performance can be achieved in these types of ILEs which is attributed to the interface-stabilising properties of ILE and the formation of a beneficial CEI on Ni-rich positive electrodes.<sup>[24]</sup>

The electrochemical performance of lithium-ion cells using either of the two ILEs was further investigated. The full-cell were balanced with a Negative/Positive capacity ratio of ~1.2. To prevent Li plating on the negative electrode and extreme delithiation of the positive electrode, the voltage window was limited to 2.6–4.1 V. The voltage profiles in Figure 3 display the typical response of SiG||NCM88 lithium-ion cells and are recorded at 0.2 C. In Figure 3(a) the polarisation gradually increases upon cycling in ILE1, which could be due to the unstable electrode-electrolyte interphases and internal resistance increase. On the contrary, the polarisation only slightly increases in ILE2. The corresponding differential capacity plots are shown in Figure S6. The anodic redox features appear to be reversible in ILE2, while a substantial loss of redox activity and a strong shift of the feature around 3.6 V is observed in ILE1, which might reflect the structural degradation of the active materials.<sup>[38]</sup> Although both electrolyte systems show a gradual capacity decay, the capacity retention after 200 cycles is much higher for the cell using ILE2 (51.7% vs. 73.8%, respectively). The fading is likely associated to the relatively low CE, i.e., irreversible Li losses in repeated SEI formation on the Si (and graphite) surface after rupture due to the large volume expansion of the Si fraction and exfoliation of graphite in the composite.<sup>[39]</sup> Besides, the structural and morphological degra-

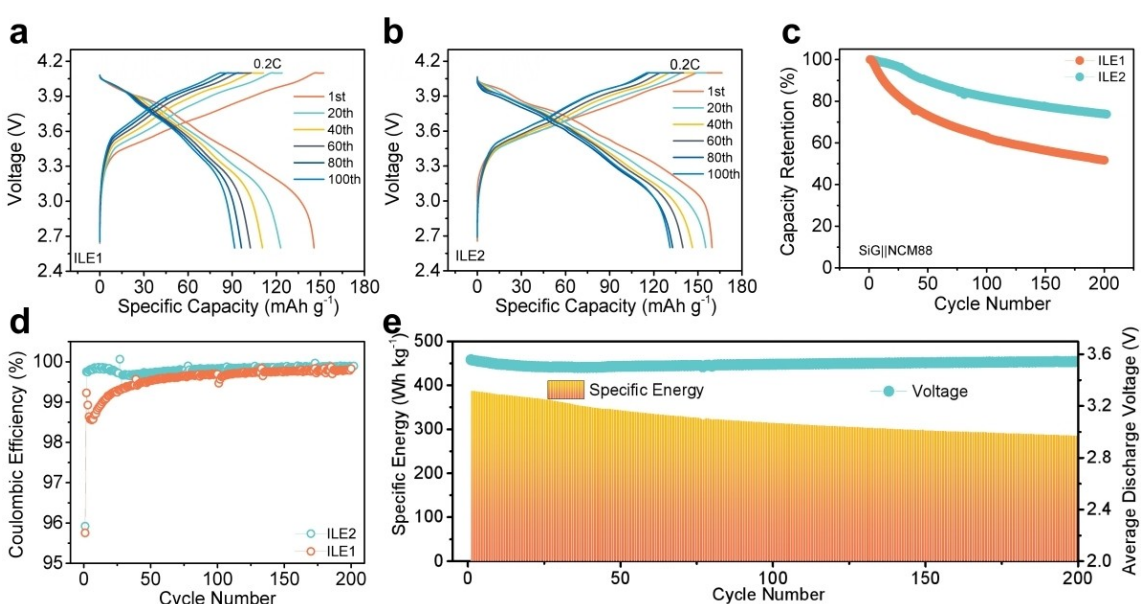


**Figure 3.** Selected voltage profiles of SiG||NCM88 lithium-ion cells at 0.2 C in a) ILE1 and b) ILE2. c) Capacity retention and d) corresponding CE of the lithium-ion cells tested in both ILEs. e) Specific energy and average discharge voltage of a SiG||NCM88 lithium-ion cell in ILE2. The specific capacity refer to weight of NCM88 only and the specific energy values refer to the weight of NCM88 and SiG.

dation of the positive electrode might also affect the full-cell performance. Figure 3d compares the average CE of both lithium-ion full-cells, which in the early stages is clearly lower (98.5%) for ILE1, before it gradually increases to 99.0%. This indicates more severe Li loss during the first few cycles and is reflected in the rapidly fading capacity. In ILE2, a notably higher average CE of 99.8% was achieved yet from the initial cycles, which is not only higher than for ILE1, but also on a similar level as for the OR electrolyte with fine-tuned additives. Consequently, Figure 3(e) displays the average discharge voltage of the SiG || NCM88 lithium-ion cell using ILE2, which is extremely stable and close to 3.6 V. In addition, the first discharge capacity is 166 mAh g<sup>-1</sup> at 0.2 C, corresponding to a high specific energy of 385 Wh kg<sup>-1</sup>, which is an excellent value for an ILE-based LIB using SiG negative and high Ni content positive electrode. More importantly, a high specific energy of 300 Wh kg<sup>-1</sup> could be maintained throughout 200 cycles, which confirms a good stability that could potentially meet the requirement for electric vehicle application.<sup>[40]</sup> Electrochemical impedance spectroscopy measurements further demonstrated the effect of ILE2 on the stability of the electrode-electrolyte interface, as shown in Figure S7, which includes the SEI/CEI film resistance ( $R_f$ ) and the charge transfer resistance ( $R_{ct}$ ) of the cathode and anode electrode. Upon cycling, i.e., after 10 and 20 cycles, the full-cell shows rather low and stable impedance. These results suggest that ILE2 can stabilise the electrode-electrolyte interfaces of both the electrodes improving the long-term cycling performance of the high-energy lithium-ion cells.

To elucidate the mechanism of enhanced lithium-ion cell performance in ILEs, an in-depth SEM analysis was carried out to investigate the structural evolution of the active materials after 200 cycles. The SEM images of cycled SiG electrodes in

both ILEs are shown in Figure 4, serious exfoliation of the graphite layers can be seen for ILE1, which might be attributed to an unstable SEI. The co-insertion of solvent molecules together with Li-ions exfoliates the graphite layer. In contrast, the graphite and Si particles of SiG electrodes cycled in ILE2 still show the original flake-like morphology and no pulverisation of Si (Figure S8). This highlights the favourable impact of the mixed anions of FSI<sup>-</sup> and TFSI<sup>-</sup> with high electrochemical stability during repeated de-/lithiation.

A comparably striking difference is observed for the positive electrodes recovered after cycling. Figure 5 depicts top view and cross-section SEM images after focused-ion beam (FIB) milling. From the top view (Figure 5a, d, g), all the samples have a similar morphology without any evident cracks or fracture of the secondary particles surrounded by carbon black. However, at the interior of the particles, the picture is completely different. The fresh electrode has a well-structured shape with no microcracks between the clearly visible primary particle grains. Whereas the secondary particles cycled in ILE1 have several cracks inside their core, due to the strong anisotropic strain of the crystal lattice when lithium ions are extracted during charging.<sup>[40]</sup> On the contrary, the microcracks in NCM88 cycled in ILE2 are significantly reduced, if not absent, suggesting that a stable CEI is formed that protects the secondary particles' structure. Taken together these findings highlight the importance of the electrolyte, which appears to dictate the evolution of the morphology of the active materials in both positive and negative electrode and thus strongly affects the electrochemical performance.

To explicate the nature of the different electrochemical performance and how the two ILEs affect the morphology of the active material particles, the surface chemistry compositions of cycled SiG and NCM88 electrodes were investigated by

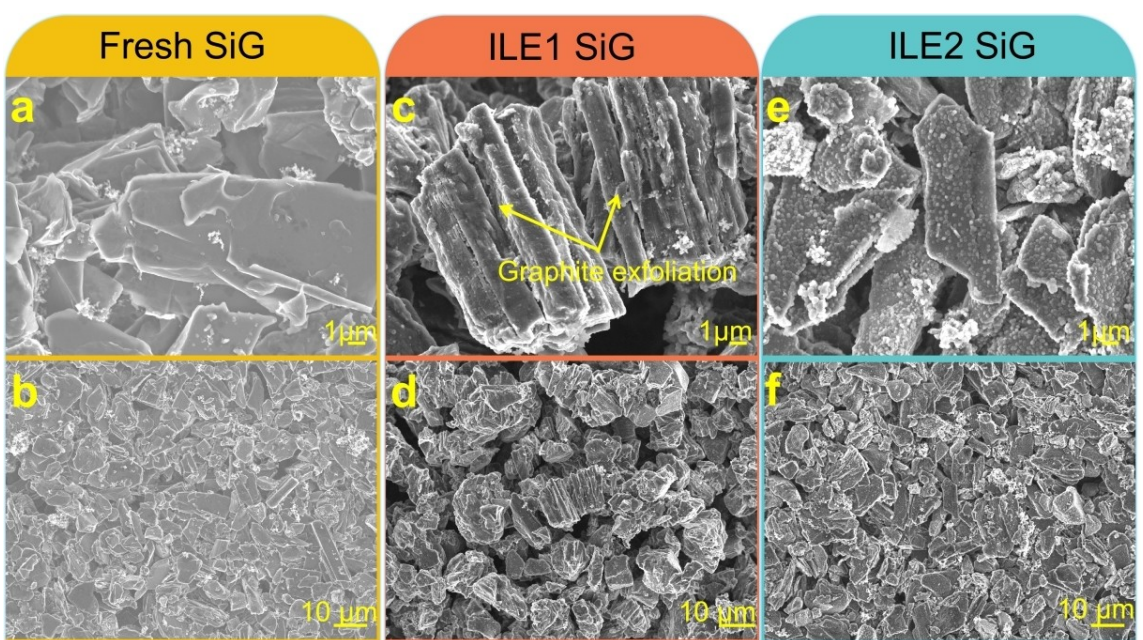
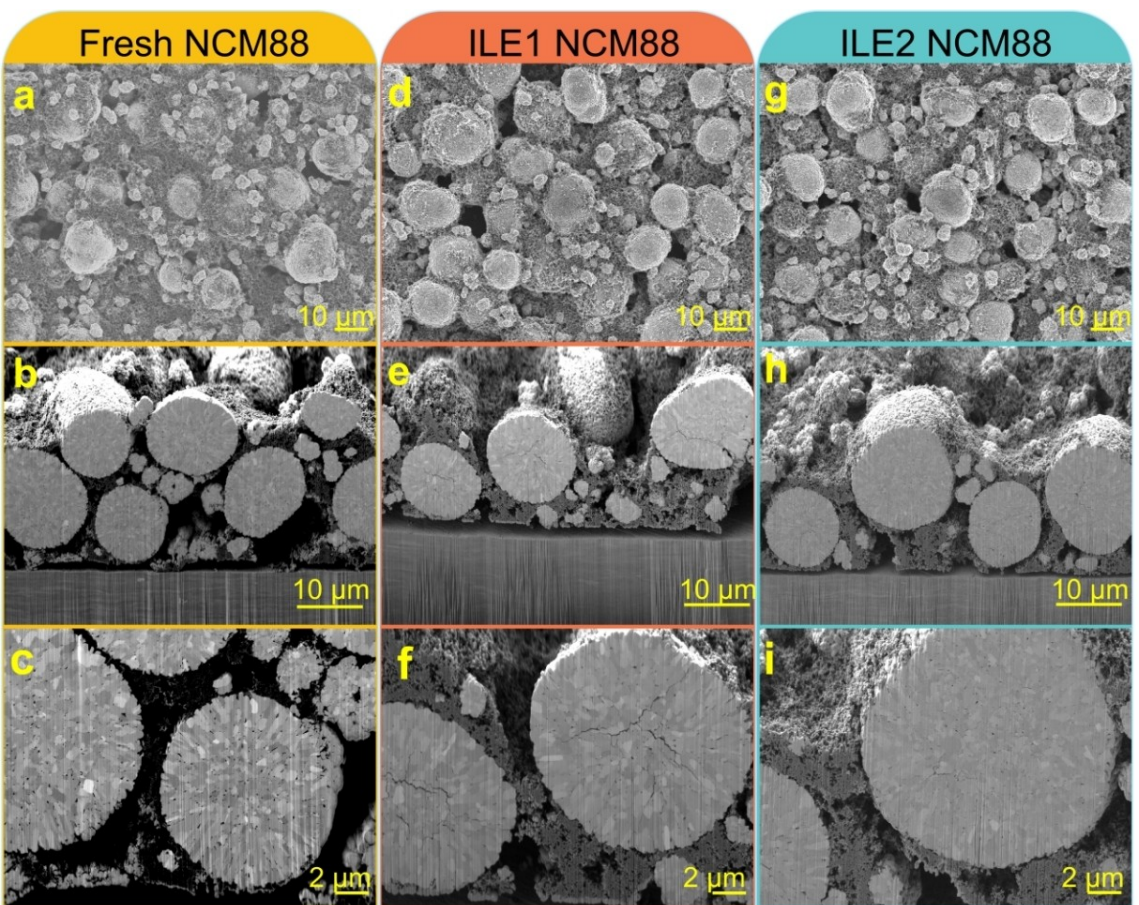


Figure 4. SEM images of a, b) as made and c–f) cycled SiG electrodes recovered from lithium-ion cells after 200 cycles in (c, d) ILE1 and (e, f) ILE2.



**Figure 5.** Top view SEM images and corresponding cross-sectional FIB-SEM images of a–c) pristine NCM88 electrodes and d–i) electrodes recovered from lithium ion-cells after 200 cycles d–f) in ILE1 and in g–i) in ILE2.

X-ray photoelectron spectroscopy (XPS). According to the literature, the  $\text{Li}^+$  cation is preferentially coordinated by  $\text{TFSI}^-$  instead of  $\text{FSI}^-$ , which is expected to be true for the charge/discharge process and therefore reflected in the chemistries of both the SEI and CEI.<sup>[42,43]</sup> Figure 6 compares the XPS spectra, before and after sputtering 3 and 10 min of SiG anodes after 200 cycles in either electrolyte recovered from the lithium-ion cells. For ILE1 (Figure 6a), the O 1s spectrum has two components at 532.4 and 531.3 eV, which correspond to  $-\text{C}-\text{O}-\text{C}-/\text{S}=\text{O}$  and  $-\text{C}=\text{O}$ , respectively.<sup>[44]</sup> In the C 1s region, the peaks characteristic for  $-\text{CO}_3^{2-}$  (289.0 eV),  $-\text{C}-\text{O}-\text{C}-/\text{C}-\text{N}-$  (286.3 eV) and  $-\text{C}-\text{C}-/\text{C}-\text{H}-$  (284.8 eV)<sup>[45]</sup> are observed, which is consistent with the O 1s spectrum. Interestingly, the C 1s region does not show  $-\text{C}-\text{F}$  bonding from FEC at high binding energies ( $> 290$  eV)<sup>[46]</sup> indicating the FEC reduction by  $\text{F}^-$  release and ring-opening forming  $-\text{C}-\text{O}-\text{C}-$  polymeric species.<sup>[47,48]</sup> This agrees with the F 1s region, where two signals are observed, which correspond to  $\text{FSI}^-$  and  $\text{LiF}$  inorganic species. The latter one formed from  $\text{FSI}^-$  and FEC reduction.<sup>[49,50]</sup> This is supported by the N 1s spectrum, where  $\text{FSI}^-$  contribution is observed at 399.5 eV, as well as  $\text{Li}_3\text{N}$  from  $\text{FSI}^-$  reduction.<sup>[51]</sup> In addition,  $\text{Pyr}_{14}^+$  traces are shown at 402.3 eV. Finally, the S 2p region provides more details about IL fragments, such as,  $\text{FSI}^-$ ,  $\text{FNSO}_2^-/\text{SO}_4^{2-}$  and  $\text{SO}_3^{2-}$  ( $\text{Li}_2\text{SO}_3$ ) at

169.8, 168.7, and 166.8 eV, respectively.<sup>[52,53]</sup> After 3 and 10 min of sputtering, the chemical species and their relative concentration remains practically unchanged, indicating that a significant amount of IL is trapped on the SEI, with a thick SEI being formed that is chemically homogeneous at higher depths. A thicker SEI may increase the resistance of the electrode and cause sluggish  $\text{Li}^+$  transport kinetics contributing to capacity fading.

On the other hand, even though the SEI of the SiG electrode cycled in ILE2 (Figure 6b) is composed of similar species as in ILE1, such as  $-\text{COC}-$ ,  $-\text{C}=\text{O}$  ( $\text{Li}_2\text{CO}_3$ ),  $\text{LiF}$ ,  $\text{Li}_3\text{N}$ ,  $\text{NFSO}_2^-$  and  $\text{Li}_2\text{SO}_3$ , different concentrations are observed. In addition,  $\text{ROCO}_2\text{Li}$ ,  $\text{Li}_2\text{O}$ , and  $\text{Li}_x\text{C}_y$  species are also formed in ILE2 SEI, as the O 1s and C 1s spectra indicated.<sup>[44,45]</sup> Moreover, the spectra after 3 and 10 min of the sputtering indicate that the SEI species distribution is not homogeneous as in ILE1 SEI. In fact, the oxygen-carbon species, such as  $-\text{C}-\text{O}-\text{C}-$ , and  $\text{ROCO}_2\text{Li}$ , as well as low concentration of ILE2 traces ( $\text{Pyr}_{14}^+$  and  $\text{TFSI}^-/\text{FSI}^-$ ) are mainly observed on the outermost layer of the SEI, while the sublayer (close to SiG electrode) is composed of inorganic-rich species, i.e.,  $\text{Li}_2\text{O}$ ,  $\text{Li}_2\text{CO}_3$  ( $-\text{C}=\text{O}$ ),  $\text{Li}_x\text{C}_y$ ,  $\text{LiF}$  and  $\text{Li}_3\text{N}$ . Moreover, the ILE2 SEI is overall richer in inorganic species, which provides high ionic conductivity, superior Li ion diffusion and electrochemical performance.<sup>[54]</sup>

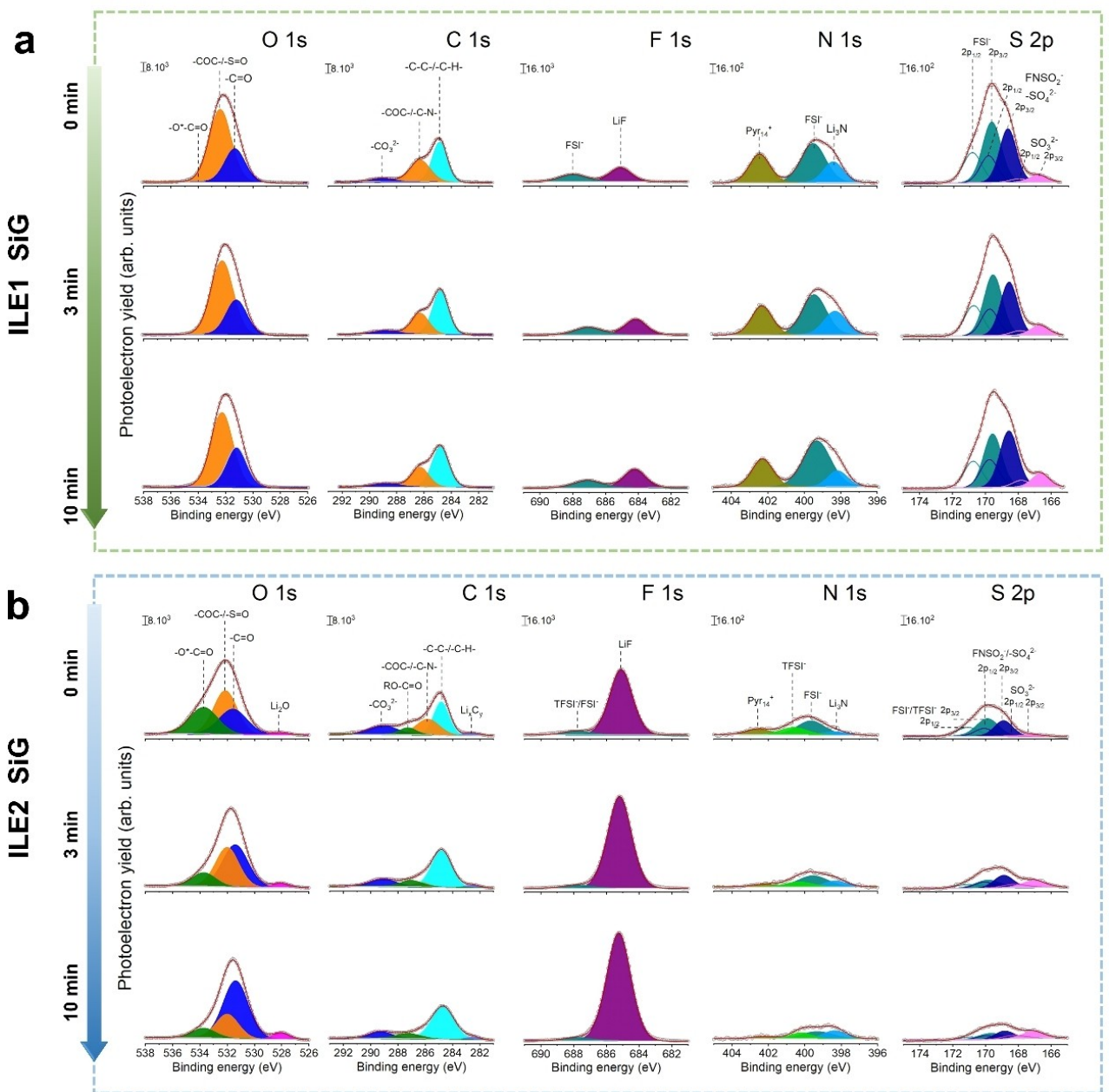


**Figure 6.** High-resolution core level XPS of the O 1s, C 1s, F 1s, N 1s and S 2p region of SiG electrodes recovered from SiG | NCM88 lithium-ion cells after 200 cycles in a) ILE1 and b) ILE2. The time scale on the left indicates times for  $\text{Ar}^+$  sputtering to remove the outer layers of the SEI and electrode ( $0.8 \text{ nm min}^{-1}$ ) and probe the depth profile.

Figure 7 depicts the comparison of the CEI chemical composition on the NCM88 positive electrodes after cycling. The deconvolution of the O 1s spectra of the electrodes cycled in ILE1 and ILE2 show components at 529.5, 531.8, 532.5 and 533.8 eV, which correspond to M–O (M=Ni, Co, Mn), and –C=O, –S=O–C–O–C–, –O\*–C=O,  $\text{Li}_2\text{CO}_3$ , FSI/TFSI/ethers and  $\text{RCO}_2\text{Li}$ , respectively. After sputtering (3 and 10 min) the concentration of carbonates (–C=O) increase in both ILE systems. Furthermore, the M–O peak, which corresponds to NCM88, is more pronounced in the ILE2 CEI, suggesting a thinner CEI. In addition, the C 1s region in both configurations shows the same trend as O 1s, displaying peaks which correspond to

–C–C–/–C–H– (conductive carbon and hydrocarbons), –C–O–C– (ether from FEC ring opening)/–C–N– (citation of ILE)/–CH<sub>2</sub> (PVdF), –O–C=O (ROCO<sub>2</sub>Li) and –CO<sub>3</sub><sup>2-</sup> (Li<sub>2</sub>CO<sub>3</sub>)/–CF<sub>2</sub> (PVdF, FEC and/or FSI/TFSI).<sup>[53]</sup> The comparison of the F 1s, N 1s and S 2p spectra of cycled NCM88 and SiG electrodes shows that the ILEs are decomposed to a lesser extent at cathode side than the anode side, not forming inorganic-rich CEIs. The ILE2 CEI exhibits low concentration of LiF, which may be due to less decomposition of FEC and FSI<sup>-</sup>/TFSI<sup>-</sup> anions. This is expected since TFSI<sup>-</sup> prefers to absorb at the electrode and hence displaces a fraction of FSI<sup>-</sup> from the surface, therefore, the relatively slower reaction of TFSI<sup>-</sup> helps to control the FSI<sup>-</sup>

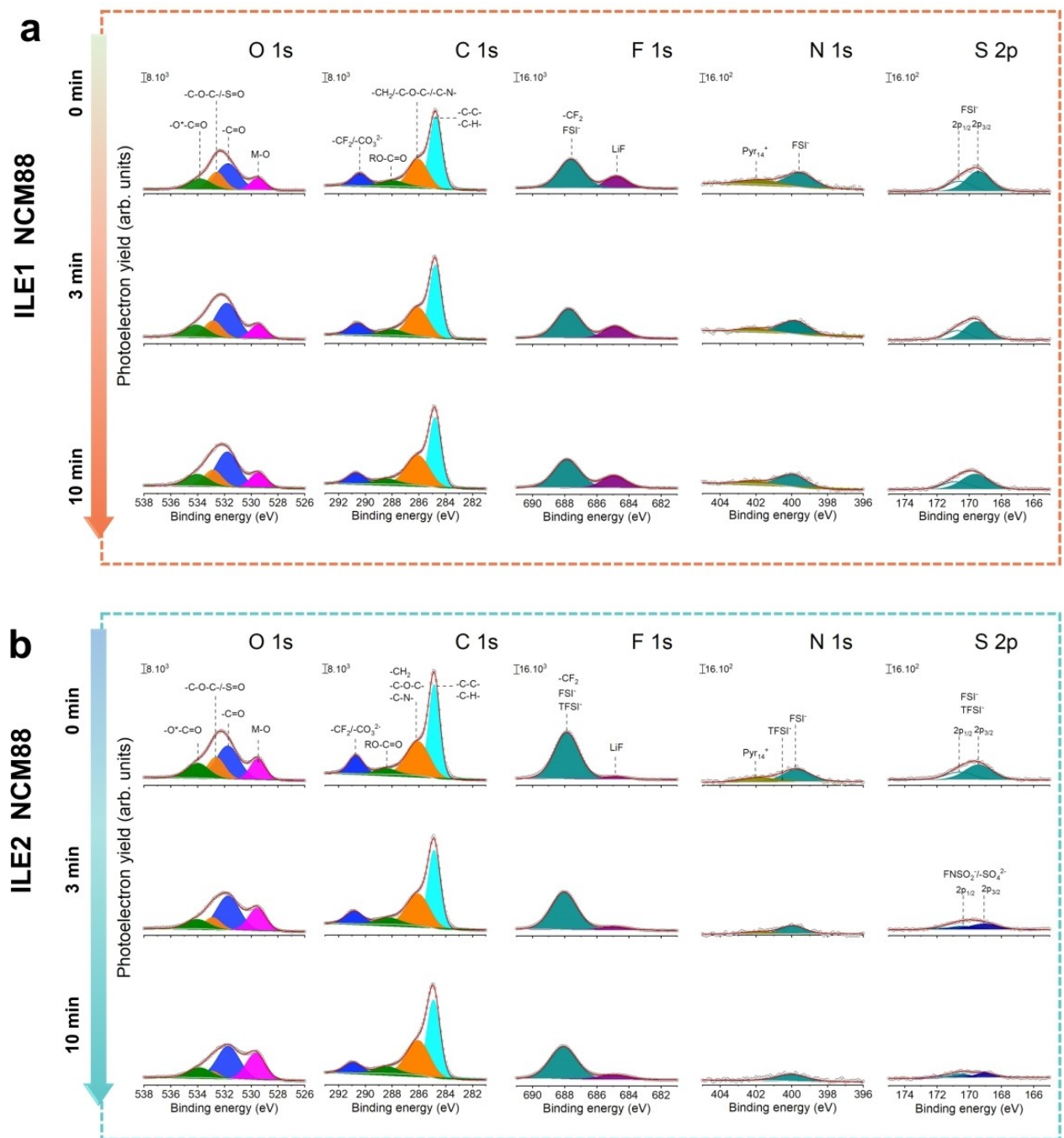


**Figure 7.** High-resolution core level XPS of the O 1s, C 1s, F 1s, N 1s and S 2p spectra of NCM88 electrodes recovered from SiG | NCM88 lithium-ion cells after 200 cycles in a) ILE1 and b) ILE2. The time scale on the left indicates times for  $\text{Ar}^+$  sputtering to remove the outer layers of the CEI and electrode ( $0.8 \text{ nm min}^{-1}$ ) and probe the depth profile.

decomposition kinetics.<sup>[42]</sup> As a result, less LiF and other  $\text{FSI}^-$ /TFSI<sup>-</sup> reduction products accumulate on the surface, leading to the formation of a more uniform and robust CEI.<sup>[42]</sup>

In summary, single-anion ILE forms a thick SEI and CEI, which potentially leads to rapidly increasing cell impedance, accelerating the growth of cell polarisation as observed in Figure 3, and resulting in a rapid capacity decay. On the contrary, the dual anion electrolyte (ILE2) possesses an SEI composed of chemically different layers, i.e., organic-rich outer-

most and inorganic-rich sublayer, while thinner CEI is formed with respect to ILE1, due to the lower decomposition of the FSI/TFSI and FEC on the cathode side. The different SEI and CEI properties on the ILE2 system may be optimal for a superior electrode protection, since NCM88 shows reduced crack formation, and SiG does not show graphite exfoliation and pulverisation of Si during cycling.

## Conclusion

In this work, the stable cycling of high specific energy LIBs comprised of NCM88 (Ni-rich) positive electrodes and SiG negative electrodes were demonstrated using an IL-based electrolyte. Lithium-ion cells employing ILE2 (0.2 mol LiTFSI-0.8 mol Pyr<sub>14</sub>FSI-FEC) delivered a high specific energy of 385 Wh kg<sup>-1</sup> based on both positive and negative active materials weight with a capacity retention of 74% after 200 cycles. The enhanced performance is ascribed to the different electrode-electrolyte interphase properties elucidated for ILE2. The SEI is composed of an inorganic-rich sublayer and organic outermost layer while NCM88 is covered by thin CEI. Consequently, the structural degradation and particle cracking of the Ni-rich material as well as the pulverisation of the micro-metre-sized Si could be effectively mitigated. Moreover, the graphite fraction displays high compatibility with ILE2 and does not exfoliate. Our findings highlight the potential use of such IL-based electrolyte to develop high energy density and safer LIBs making full use of state-of-the-art positive and negative electrode materials.

## Acknowledgements

The authors would like to acknowledge the financial support from the National Natural Science Foundation of China (52002176, 52161039) project, Jiangxi Provincial Natural Science Foundation (2021BAB214054), and the Helmholtz Association. Open Access funding enabled and organized by Projekt DEAL.

## Conflict of Interest

The authors declare no conflict of interest.

## Data Availability Statement

The data that support the findings of this study are available on request from the corresponding author. The data are not publicly available due to privacy or ethical restrictions.

**Keywords:** ionic liquid-based electrolyte · lithium-ion battery · Ni-rich NCM cathode · Si/graphite anode · solid electrolyte interphase

- [1] M. Winter, B. Barnett, K. Xu, *Chem. Rev.* **2018**, *118*, 11433.
- [2] F. Wu, J. Maier, Y. Yu, *Chem. Soc. Rev.* **2020**, *49*, 1569.
- [3] G. Bieker, M. Winter, P. Bieker, *Phys. Chem. Chem. Phys.* **2015**, *17*(14), 8670.
- [4] X. Zuo, J. Zhu, P. Müller-Buschbaum, Y.-J. Cheng, *Nano Energy* **2017**, *31*, 113.
- [5] K. Feng, M. Li, W. Liu, A. G. Kashkooli, X. Xiao, M. Cai, Z. Chen, *Small* **2018**, *14*, 1702737.
- [6] E. Radvanyi, W. Porcher, E. De Vito, A. Montani, S. Franger, S. Jouanneau Si Larbi, *Phys. Chem. Chem. Phys.* **2014**, *16*, 17142–17153.

- [7] B. Key, R. Bhattacharyya, M. Morcrette, V. Seznec, J. M. Tarascon, C. P. Grey, *J. Am. Chem. Soc.* **2009**, *131*, 9239.
- [8] H. Wu, Y. Cui, *Nano Today* **2012**, *7*, 414.
- [9] H. Shang, Z. Zuo, L. Yu, F. Wang, F. He, Y. Li, *Adv. Mater.* **2018**, *30*, e1801459.
- [10] X. Shen, Z. Tian, R. Fan, L. Shao, D. Zhang, G. Cao, L. Kou, Y. Bai, *J. Energy Chem.* **2018**, *27*, 1067.
- [11] H. Wang, J. Fu, C. Wang, J. Wang, A. Yang, C. Li, Q. Sun, Y. Cui, H. Li, *Energy Environ. Sci.* **2020**, *13*, 848.
- [12] Z. Xu, J. Yang, T. Zhang, Y. Nuli, J. Wang, S.-i. Hirano, *Joule* **2018**, *2*, 950.
- [13] J. Asenbauer, T. Eisenmann, M. Kuenzel, A. Kazzazi, Z. Chen, D. Bresser, *Sustain. Energy Fuels* **2020**, *4*(11), 5387.
- [14] M. Armand, P. Axmann, D. Bresser, M. Copley, K. Edstrom, C. Ekberg, D. Guyomard, B. Lestriez, P. Novak, M. Petraníkova, W. Porcher, S. Trabesinger, M. W. Mehren, H. Zhang, *J. Power Sources* **2020**, *479*, 228708.
- [15] H.-H. Ryu, K.-J. Park, C. S. Yoon, Y.-K. Sun, *Chem. Mater.* **2018**, *30*, 1155.
- [16] C. S. Yoon, M. H. Choi, B.-B. Lim, E.-J. Lee, Y.-K. Sun, *J. Electrochem. Soc.* **2015**, *162*(14), A2483.
- [17] D. S. Ko, J. H. Park, B. Y. Yu, D. Ahn, K. Kim, H. N. Han, W. S. Jeon, C. Jung, A. Manthiram, *Adv. Energy Mater.* **2020**, *10*, 2001035.
- [18] H. Cha, J. Kim, H. Lee, N. Kim, J. Hwang, J. Sung, M. Yoon, K. Kim, J. Cho, *Adv. Mater.* **2020**, *32*, e2003040.
- [19] Z. Huang, J. Gao, X. He, J. Li, C. Jiang, *J. Power Sources* **2012**, *202*, 284.
- [20] J. U. Choi, N. Voronina, Y. K. Sun, S. T. Myung, *Adv. Energy Mater.* **2020**, *10*, 2002027.
- [21] S. S. Zhang, *Energy Storage Mater.* **2020**, *24*, 247.
- [22] J. Kim, H. Ma, H. Cha, H. Lee, J. Sung, M. Seo, P. Oh, M. Park, J. Cho, *Energy Environ. Sci.* **2018**, *11*, 1449.
- [23] A. Heist, S. Hafner, S.-H. Lee, *J. Electrochem. Soc.* **2019**, *166* (6), A873.
- [24] F. Wu, S. Fang, M. Kuenzel, A. Mullalui, J.-K. Kim, X. Gao, T. Diemant, G.-T. Kim, S. Passerini, *Joule* **2021**, *5*, 2177.
- [25] M. Ishikawa, T. Sugimoto, M. Kikuta, E. Ishiko, M. Kono, *J. Power Sources* **2006**, *162*, 658.
- [26] H. Zheng, K. Jiang, T. Abe, Z. Ogumi, *Carbon* **2006**, *44*, 203.
- [27] N. Yabuuchi, K. Shimomura, Y. Shimbe, T. Ozeki, J.-Y. Son, H. Oji, Y. Katayama, T. Miura, S. Komaba, *Adv. Energy Mater.* **2011**, *1*, 759.
- [28] E. Peled, S. Menkin, *J. Electrochem. Soc.* **2017**, *164*, A1703.
- [29] X. Li, A. M. Colclasure, D. P. Finegan, D. Ren, Y. Shi, X. Feng, L. Cao, Y. Yang, K. Smith, *Electrochim. Acta* **2019**, *297*, 1109.
- [30] D. Anseán, G. Baure, M. González, I. Cameán, A. B. García, M. Dubarry, *J. Power Sources* **2020**, *459*, 22782.
- [31] Y. Jin, N. H. Kneusels, P. Magusin, G. Kim, E. Castillo-Martinez, L. E. Marbella, R. N. Kerber, D. J. Howe, S. Paul, T. Liu, C. P. Grey, *J. Am. Chem. Soc.* **2017**, *139*, 14992.
- [32] B. Han, Y. Zou, G. Xu, S. Hu, Y. Kang, Y. Qian, J. Wu, X. Ma, J. Yao, T. Li, Z. Zhang, H. Meng, H. Wang, Y. Deng, J. Li, M. Gu, *Energy Environ. Sci.* **2021**, *14*, 4882.
- [33] G. A. Elia, U. Ulissi, S. Jeong, S. Passerini, J. Hassoun, *Energy Environ. Sci.* **2016**, *9*, 3210.
- [34] Z. Feng, K. Higa, K. S. Han, V. Srinivasan, *J. Electrochem. Soc.* **2017**, *164*, A2434.
- [35] N. Sanchez-Ramirez, B. D. Assresahgen, R. M. Torresi, D. Bélanger, *Energy Storage Mater.* **2020**, *25*, 477.
- [36] N. Xiao, G. Gourdin, Y. Wu, *Angew. Chem. Int. Ed.* **2018**, *57*, 10864.
- [37] W. Xue, Z. Shi, M. Huang, S. Feng, C. Wang, F. Wang, J. Lopez, B. Qiao, G. Xu, W. Zhang, Y. Dong, R. Gao, Y. Shao-Horn, J. A. Johnson, J. Li, *Energy Environ. Sci.* **2020**, *13*, 221.
- [38] H. H. Ryu, G. T. Park, C. S. Yoon, Y. K. Sun, *J. Mater. Chem. A* **2019**, *7*, 18580.
- [39] T. Yoon, C. C. Nguyen, D. M. Seo, B. L. Lucht, *J. Electrochem. Soc.* **2015**, *162*(12): A2325.
- [40] X. Zeng, M. Li, D. Abd El-Hady, W. Alshitar, A. S. Al-Bogami, J. Lu, K. Amine, *Adv. Energy Mater.* **2019**, *9*, 1900161.
- [41] J. H. Kim, S. J. Kim, T. Yuk, J. Kim, C. S. Yoon, Y.-K. Sun, *ACS Energy Lett.* **2018**, *3*, 3002.
- [42] J. Alvarado, M. A. Schroeder, T. P. Pollard, X. Wang, J. Z. Lee, M. Zhang, T. Wynn, M. Ding, O. Borodin, Y. S. Meng, K. Xu, *Energy Environ. Sci.* **2019**, *12*, 780.
- [43] V. Lesch, S. Jeremias, A. Moretti, S. Passerini, A. Heuer, O. Borodin, *J. Phys. Chem. B* **2014**, *118*, 7367.
- [44] A. M. Andersson, A. Henningson, H. Siegbahn, U. Jansson, K. Edstrom, *J. Power Sources* **2003**, *119*, 522.
- [45] R. I. R. Blyth, H. Buqa, F. P. Netzer, M. G. Ramsey, J. O. Besenhard, G. Golob, M. Winter, *Appl. Surf. Sci.* **2000**, *167*, 99.

- [46] C. D. Wagner, W. M. Riggs, L. E. Davis, J. F. Moulder, G. E. Muilenberg, *Handbook of X-ray Photoelectron Spectroscopy*, Perkin-Elmer Corp. 1979.
- [47] L. Vogganis, W. Heitz, *Rapid Commun.* **1986**, *7*(9), 543.
- [48] Y. Jin, N. J. H. Kneusels, L. E. Marbella, E. C. Martinez, P. C. Magusin, R. S. Weatherup, E. Jonsson, T. Liu, S. Paul, C. P. Grey, *J. Am. Chem. Soc.* **2018**, *140*, 9854.
- [49] F. Wu, G. T. Kim, T. Diermant, M. Kuenzel, A. R. Schür, X. Gao, B. Qin, D. Alwast, Z. Jusys, R. J. Behm, D. Geiger, U. Kaiser, S. Passerini, *Adv. Energy Mater.* **2020**, *10*, 2001830.
- [50] Z. Chen, G. T. Kim, J. K. Kim, M. Zarabeitia, M. Kuenzel, H. P. Liang, D. Geiger, U. Kaiser, S. Passerini, *Adv. Energy Mater.* **2021**, *11*, 2101339.
- [51] H. Kim, F. Wu, J. T. Lee, N. Nitta, H. T. Lin, M. Oschatz, W. I. Cho, S. Kaskel, O. Borodin, G. Yushin, *Adv. Energy Mater.* **2015**, *5*, 1401792.
- [52] W. Xue, Z. Shi, M. Huang, S. Feng, C. Wang, F. Wang, J. Lopez, B. Qiao, G. Y. Xu, W. X. Zhang, Y. H. Dong, R. Gao, S. H. Yang, J. A. Johnson, J. Li, *Energy Environ. Sci.* **2020**, *13*, 212.
- [53] K. Park, J. B. Goodenough, *Adv. Energy Mater.* **2017**, *7*, 1700732.
- [54] K. Kim, Y. Kim, S. Park, H. J. Yang, S. J. Park, K. Shin, J. J. Woo, S. Kim, S. Y. Hong, N.-S. Choi, *J. Power Sources* **2018**, *396*, 276.

Manuscript received: June 27, 2022  
Revised manuscript received: June 30, 2022  
Accepted manuscript online: July 4, 2022  
Version of record online: July 21, 2022